Leaf-Like TENGs for Harvesting Gentle Wind Energy at An Air Velocity as Low as 0.2 m s⁻¹

Hao Li, Jing Wen, Zhiqiang Ou, Erming Su, Fangjing Xing, Yuhan Yang, Yanshuo Sun, Zhong Lin Wang,* and Baodong Chen*

Existing technologies for harvesting electrical energy from gentle wind face an enormous challenge due to the limitations of cut-in and rated wind speed. Here, a leaf-like triboelectric nanogenerator (LL-TENG) is proposed that uses contact electrification caused by the damped forced vibration of topology-optimized structure consisting of flexible leaf, vein bearing plate, and counterweight piece. The effectiveness of the topology-optimized leaf-like structure is studied, which solves the problem of reduced output due to electrostatic adsorption between the leaf surfaces while reducing the cut-in (0.2 m s⁻¹) and rated wind speed (2.5 m s⁻¹). The LL-TENG unit having small dimensions of 40 cm⁻² (mass of 9.7 g) at a gentle wind of 2.5 m s⁻¹ exhibits outstanding electrical performances, which produces an open-circuit voltage of 338 V, a short-circuit current of 7.9 µA and the transferred charge density of 62.5 µC m⁻² with a low resonant frequency of 4 Hz, giving an instantaneous peak power of 2 mW. A distributed power source consists of the five LL-TENGs in parallel is developed by designed self-adaptive structure, for which the peak power output reaches 3.98 mW, and its practicability and durability are successfully demonstrated. This study is a promising distributed power source technology to drive electronics in gentle wind outdoor environments.

1. Introduction

Wind is a vast, clean, readily available, and renewable energy source, which is used to produce electricity using the kinetic energy created by air in motion. General wind classifications are divided into 12 Beaufort-Wind-Scale for differentiating winds of different average speeds such as calm, light air, breeze, gale, storm, and hurricane. Wind is harvested through wind turbines or energy conversion devices, which generate electricity by converting the kinetic energy of the wind into mechanical energy.[1] Gentle wind (calm, light air, and breeze) is a more random and intermittent source of energy which occupies the major proportion in the whole year of wind distribution and an important role in energy collection. For example, simple and high-efficiency harvesting gentle wind energy enjoys huge potential and broad prospect in outdoor or desert.[2] However, traditional electromagnetic technologies for harvesting electrical energy from gentle wind face an enormous challenge due to the limitations of cut-in and rated wind speed, and continual emerged new technologies often fail to displace old ones or as a useful supplement.

TENGs (triboelectric nanogenerators)[3] were shown that the technologies possess high-effective conversation of the random low-frequency mechanical energy into electricity, such as wind,[4] raindrops,[5] water waves,[6] and biomechanical energy. Because of several advantages it offers over other distributed energy harvesting technologies, which are easy fabrication,[7] lightweight,[8] low cost,[9] diverse selection of materials,[10] and strong adaptability. Therefore, a variety of TENG prototypes have been developed using for collecting different speeds of wind energy by optimized device structure and triboelectric materials.[11] During the research, it was discovered that relatively few studies have been conducted on the collection of gentle wind energy. Most reports focusing on the high air velocity (>5 m s⁻¹) as a result of structural limitations of these devices resulting in the demand of high cut-in wind speeds if running fine.[7a,12] Therefore, the development of a matched TENG for high-efficiency harvesting gentle wind energy is necessary to promote the practical application and to supply the world's present energy demands.

H. Li, E. Su
Center on Nanoenergy Research
School of Physical Science and Technology
Guangxi University
Nanning 530004, P. R. China
H. Li, J. Wen, E. Su, F. Xing, Y. Yang, Y. Sun, Z. L. Wang, B. Chen
Beijing Institute of Nanoenergy and Nanosystems
Chinese Academy of Sciences
Beijing 101400, P. R. China
E-mail: zhong.wang@mse.gatech.edu; chenbaodong@binn.cas.cn
Z. Ou
Inner Mongolia Key Laboratory for Physics and Chemistry of Functional Materials
College of Physics and Electronic Information
Inner Mongolia Normal University
Hohhot 010022, P. R. China
Z. L. Wang
Georgia Institute of Technology
Atlanta, GA 30332, USA

ADVANCED
SCIENCE NEWS

www.advancedsciencenews.com

ADVANCED
FUNCTIONAL
MATERIALS

www.afm-journal.de

Here, we report a leaf-like triboelectric nanogenerator (LL-TENG) with topology-optimized leaf-like structure which can high-effectively harvest wind, airflow speeds from the range of 0.2 to 5.5 m s^{-1}. We study the effectiveness of topology-optimized strategy, which solves the problem of reduced electrical output due to electrostatic adsorption between the leaf surfaces while reducing the cut-in (0.2 m s^{-1}) and rated wind speed (2.5 m s^{-1}). The advantage of LL-TENG with ultralow cut-in wind speed is demonstrated by damped forced vibration in a topology-optimized structure. The peak power of LL-TENG unit may reach 2 mW at a wind speed of 2.5 m s^{-1}, and its practicability and durability are successful demonstrated. A distributed power consisting of five-unit LL-TENGs in parallel is developed by designed self-adaptive structure which the peak power reaches 3.98 mW that shows the advantage of LL-TENG for harvesting low-speed gentle wind energy. Coupled with an energy management system, it may be utilized as a direct-current power for driving electronics and has proved itself in applications such as a self-powered emergency alarm system and a self-powered weather monitoring network, respectively. This work proposes an efficient method for collecting the ubiquitous gentle wind that is overlooked by traditional technologies or cannot be collected owing to structural restrictions. This is crucially significant and might be a valuable addition to existing distributed power sources.

2. Results and Discussion

2.1. Structure Design and Working Principle of LL-TENG

Figure 1a shows a diagram of a distributed power source network based on the LL-TENGs array for harvesting gentle wind energy to drive electronics in the desert. General wind classifications are divided into 12 Beaufort-Wind-Scale, as shown in Table S1 (Supporting Information). The LL-TENG uses contact electrification caused by the damped forced vibration of topology-optimized structure consisting of flexible leaf, vein bearing plate, and counterweight piece, the photograph is shown in Figure 1b. The functional materials involved are 430 stainless-steel sheets, fluorinated ethylene propylene (FEP) film, aluminum (Al) film, and polyvinyl chloride (PVC) film, as shown in Figure 1c. Considering that the appropriate thickness and the mechanical properties of the material have a positive effect on the physical vibrations as well as in order to achieve an ultra-low resonance frequency, a 430 stainless-steel sheets (50 μm) was chosen as the lower support leaf surface. Its super elasticity makes it easy to deform when subjected to small pressures and to return to its original shape when the pressure is released, which is vitally important for harvesting low-speed gentle wind energy. Then, FEP film, Al film, PVC film, and leaf-like vein bearing plate are sequentially attached layer-by-layer and the stainless-steel sheet as a support layer is mounted face-to-face with the PVC film using a base made from 3D printing and UV-cured resin as a spacer. The selection of FEP film as the triboelectric layer is due to its corresponding high negative charge affinity. In addition, the stainless-steel sheet was bent initially into a semi-curved shape to provide conformal contact and separation of the two triboelectric layers during damped forced vibration.

Based on the coupling between electrification and electrostatic induction, the working principle of LL-TENG with

contact-separation mode are schematically illustrated in Figure 1d. The Al film connected to the upper flexible leaf is called electrode A, acting as both an electrode and a triboelectric layer, and the stainless-steel sheet bonded to the lower leaf is called electrode B. In addition, the FEP film is attached to electrode B and plays the role of another triboelectric material. When the device is placed in a continuous wind, the leaf surface is subjected to wind forces and the damping force of the counterweight piece on top of the leaf, causing the LL-TENG to vibrate by periodic external driving forces and the dorsal leaf-like bearing plate is an effective solution to the problem of electrostatic attraction between the two leaves. As a result, the Al film and FEP film are periodically brought into contact and separated. In the beginning, electrode A contacts the FEP film (Figure 1d, state i). Due to the stronger ability of FEP film to attract negative charges, a certain number of negative charges occur on the surface of FEP film, and the same number of positive charges appear on electrode A. With the wind effects, counterweight piece of the leaf swings to a certain angle, and electrode A separates from the FEP film (Figure 1d, state ii). According to electrostatic induction, free electrons on electrode B transfer to electrode A through the external load to balance the potential difference. Therefore, a pulsed electric current is generated from electrode A to electrode B. There follows a maximum amplitude position (Figure 1d, state iii). The combined effect of drive (wind), damping (counterweight piece), and elasticity (stainless-steel sheet), resulting in the leaf swing velocity slows down to zero. Subsequently, all external forces applied can generate resilience, which can cause the leaf to spring back in reverse. At this time, the two triboelectric materials get close to each other, and electrons flow backward through the external load (Figure 1d, state iv). Finally, electrode A contacts the FEP film again, and LL-TENG returns to the original state i. Based on this periodically damped forced vibratory motion, a continuous alternating current is generated in the external circuit. As can be seen from Figure 1e, the signal shapes of the V_{OC}, short-circuit current (I_{SC}), and transferred charge (Q_{SC}) as well as, they can reach approximately 257 V, 165 nC, and 8.2 μA at a wind speed of 2.5 m s^{-1} respectively. Cut-in wind speed, as one of the most important basic parameters, is regarded as an indicator to assess the performance of TENG. Obviously, based on the structural optimization, the cut-in wind speed of LL-TENG is 0.2 m s^{-1}, which is nearly five times less than the previous relevant work, as shown in Figure 1f.[13] Notably, the LL-TENG has limitations when it comes to collecting wind energy from all directions, since it can only do so from the oncoming wind. To achieve all-around random light-air energy harvesting, we have implemented a distributed power source consisting of five units of LL-TENG connected in parallel by a designed self-adaptive structure, as shown in Movie S1 (Supporting Information). The photographs of the distributed power source are visualized in Figure S1 (Supporting Information), which includes a left view a), a front view b), a top view c), and the 3D photograph of one single LL-TENG device d).

2.2. Vibration Model and Aerodynamic Analysis of LL-TENG

First, we equate the dynamics characteristic of LL-TENG during gentle wind-blown oscillation to a damped forced vibration
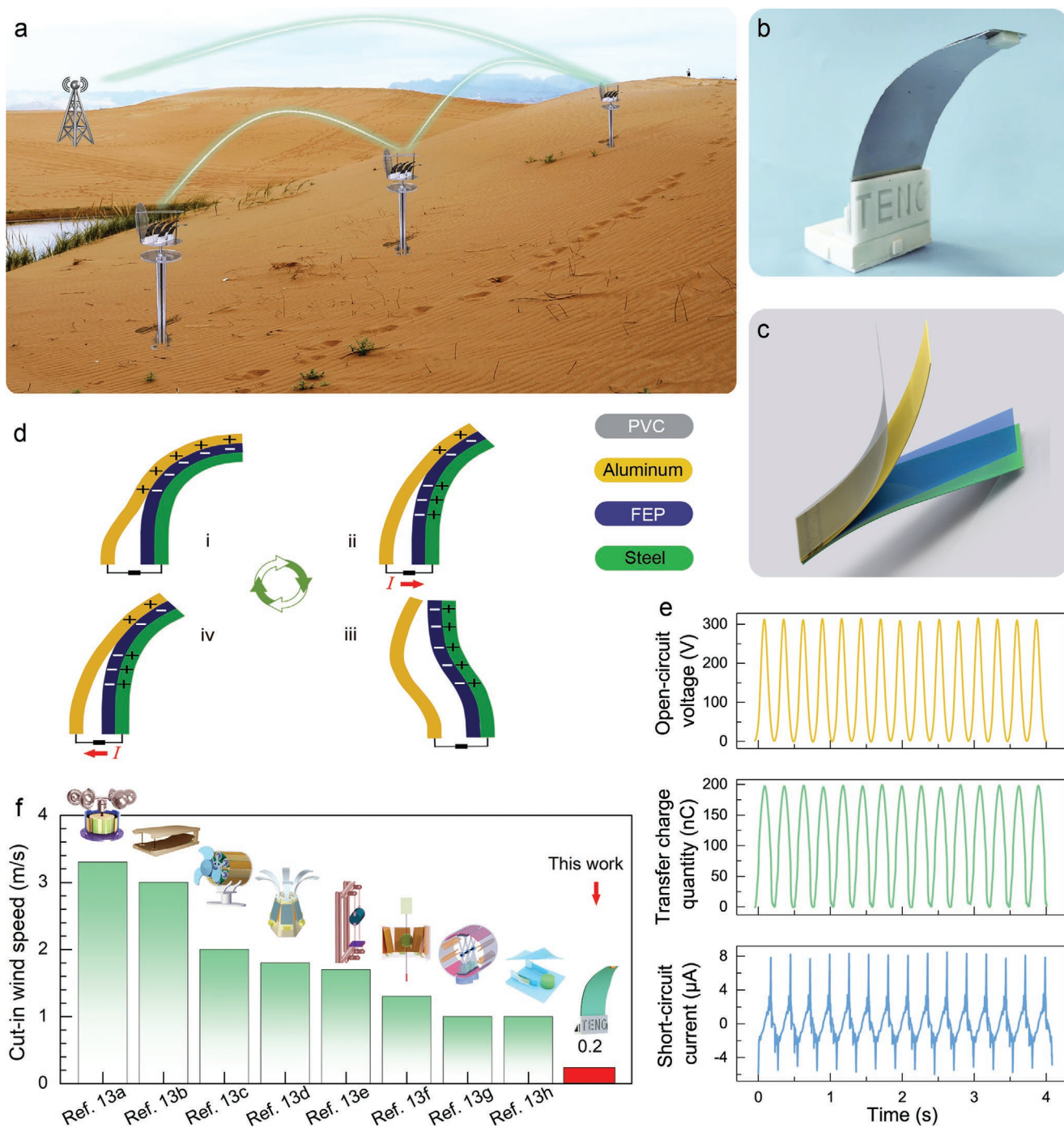
Figure 1. Application scenario, structure and working principle of LL-TENG. a) Prospective application of LL-TENG as a distributed power in the desert. b) The photograph and structure of LL-TENG. c) Working principle of LL-TENG. d) Open-circuit voltage (V_{oc}), transferred charge quantity (Q_{sc}), and short-circuit current (I_{sc}) of LL-TENG at a wind speed of 2.5 m s^{-1}. e) Bar graph of the cut-in wind speed about the comparison between the LL-TENG and existing relevant researches.

model of a mass at the top of the leaf, as shown in **Figure 2**a. In the design of LL-TENG with topology-optimized leaf-like structure, the oscillating two leaves undergo deformation and leading to its flapping. In the inset, the dynamic stress analysis of LL-TENG was simulated at the mechanical condition and external airflow conditions by using the software ANSYS, and

a finite element analyzing the interfacial stress distribution model for the topology-optimized structure of LL-TENG was set up. The results show that the dynamic stresses are concentrated at the point of contact between the leaves and the base where they increase with the amount of deformation. It is noteworthy that by optimizing the leaf radius curvature which can achieve
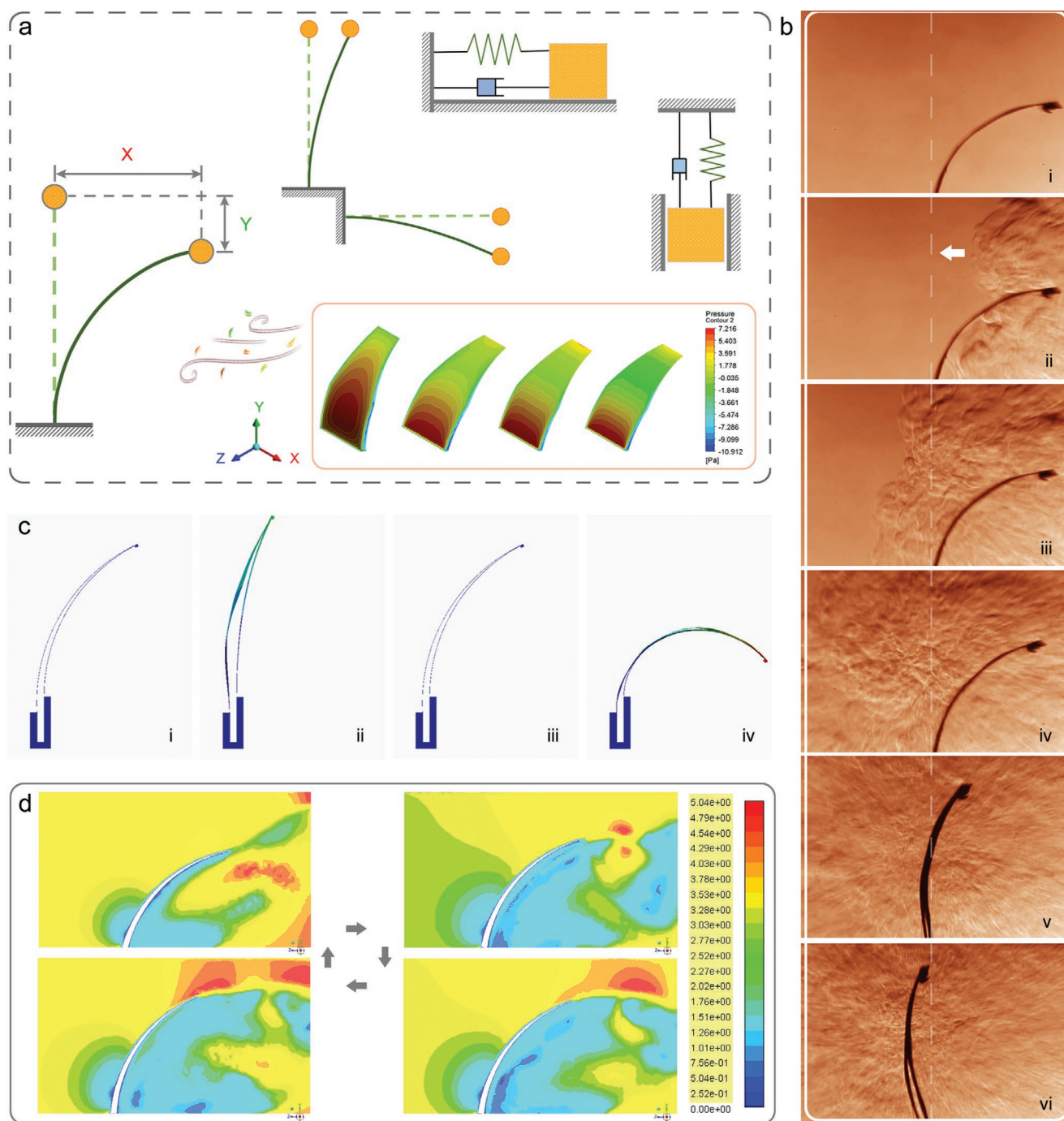
**ADVANCED
SCIENCE NEWS**

www.advancedsciencenews.com

**ADVANCED
FUNCTIONAL
MATERIALS**

www.afm-journal.de

Figure 2. Aerodynamic analysis and forced damping vibration simulation of LL-TENG. a) Simplified damped forced vibration model of LL-TENG. (Using the software ANSYS, the inset shown that the dynamic stress analysis of LL-TENG was simulated at the mechanical condition and external airflow conditions, and a finite element analyzing force model for the topology-optimized structure of LL-TENG was set up.) b) Local eddy characteristic of LL-TENG collects by schlieren photography. c) Sequential swinging features and contact-separation states of LL-TENG under the damped forced vibration. d) The simulated formation of eddies around the LL-TENG device.

the desire deformation. Based on the damped forced vibrations of the counterweight piece and the stainless-steel sheet, the vibrations on the LL-TENG are resolved into the two operating modes, the autonomous stochastic resonance induced by two modes can be determined. Thereafter, the two modes of the damped forced vibrations on the LL-TENG device are

discussed. One is the under-damped movement of the device due to the effects of rapidly changing gusts of wind over a short period of time. For example, the device is subjected to elastic and damping forces when an instantaneous wind of 3 m s^{-1} is applied to its surface in a windless state. According to the analysis of the forces analysis, the stochastic resonance system

is subjected to elastic and damping forces, which are solved by the general solution can be expressed as:

$$x = A e^{-\beta t} \cos(\omega t + \varphi) \tag{1}$$

$$A = \sqrt{x_0^2 + (v_0 + \beta x_0)^2 / \omega_0^2} \tag{2}$$

where ω_0 is the angular frequency of the stainless-steel sheet ($\omega_0^2 = k\,m^{-1}$), β is the damping coefficient, A is the amplitude and $\cos(\omega t + \varphi)$ is the period factor, details of the calculations are shown in Supporting Information Note. When $\beta < \omega_0$, the system is in underdamped forced vibration. So, it can be seen that the excitation stochastic response is related to the damping force generated by the moveable counterweight piece and that the displacement vibration curve decreases periodically with time. To verify that the experiment matches the theory, the output voltage of LL-TENG can be derived from the equivalent capacitance model of TENG as follows:

$$V_{oc} = \sigma x(t) / \varepsilon_0 \tag{3}$$

where V_{OC} is the open-circuit voltage, $x(t)$ is the transient distance between the two triboelectric layers, σ is the triboelectric electric surface charge density, and ε_0 represents the dielectric constant of the vacuum. According to the formula it can be derived that V_{OC} is proportional to the transient distance between the triboelectric layers. It is therefore possible to equate the voltage magnitude to the vibration displacement. As can be seen in Figure S2a (Supporting Information), the experimentally measured V_{OC} curve matches the calculated curve. The second mode of operation is the system being subjected to periodic external driving forced vibration. In this process, the system is subjected to three forces: the elastic force, the damping force, and the external driving force. The general solution of the formula can be expressed as:

$$x = A e^{-\beta t} \cos(\omega t + \varphi) + A \cos(\omega_p t + \varphi) \tag{4}$$

$$A = f / \sqrt{(\omega_0^2 - \omega_p^2)^2 + 4\beta^2 \omega_p^2} \tag{5}$$

where f is the external force, ω_p is the external frequency, and details of the calculations are shown in Note S1 (Supporting Information). In damped forced vibration, the vibration gains energy from the work done on it by an external force and loses energy due to damping. At the beginning of the forced vibration, the former is stronger than the latter. The vibration gradually strengthens, and as the vibration strengthens, the loss of energy increases, until the steady state is reached when the energy obtained is exactly compensated for the loss of capacity, at which time the state of motion is simple harmonic vibration. As can be seen in Figure S2b (Supporting Information), the experimentally measured V_{OC} curve matches the calculated curve. After steady state of the damped forced vibration system:

$$x = A \cos(\omega_p t + \psi) \tag{6}$$

The whole damping vibration process can be also easily decomposed into a horizontal component and a vertical component for a single degree of freedom system (Figure 2a). For the force analysis of both models, it is obtained that:

$$f_x(t) = \ddot{x} + \omega_0^2 x + 2\beta \dot{x} \tag{7}$$

$$f_y(t) = \ddot{y} + \omega_0^2 y + 2\beta \dot{y} \tag{8}$$

At the same time, the airflow distribution around the LL-TENG device can be clearly observed by the schlieren photography, as shown in Figure 2bi–vi. When the airflow starts to move on the leaf, the leaf deforms with the counterweight and the vortex can be clearly observed at the top of the leaf during the movement, as shown in Figure 2bv. Then, the interaction between the leaf and airflow was simulated via FLUNT software. Figure 2c presents the sequential images of the damped forced vibration.[14] First, the LL-TENG is showing with a certain bending on its equilibrium point, as shown in Figure 2ci. In the first half of a vibration cycle, the device first reaches the largest upward displacement, as shown in Figure 2cii; then, it returns back to the initial position, as shown in Figure 2ciii. In the remaining half cycle, the device reaches the largest downward displacement, as shown in Figure 2civ. The displacement of the device is visualized in Movie S2 (Supporting Information). The results show that the damping vibration is consistent with the simulation. As demonstrated in Figure 2d, in fluid dynamics, when an airflow past the arc-shaped elastic leaf at certain velocities, vortices are created top of the leaf, which may be one of the reasons for the wind energy harvesting achieved by LL-TENG at low speeds of wind.[15] The movement status of the LL-TENG and the formation of vortices under synchronization are shown in Figure S3 (Supporting Information). The simulation results are consistent with the airflow distribution observed by the s schlieren photography. The continuous variation of the airflow and the displacement of the leaf are visualized in Movie S3 (Supporting Information).

2.3. Structural Parameters Optimization of LL-TENG

As can be seen by ω_0, the inherent vibration of LL-TENG is related to the counterweight piece and the elasticity coefficient of the stainless-steel sheet. Thus, changing the weight of the counterweight piece can change the frequency of the damped forced vibration. Therefore, the effect of counterweight pieces was first studied. Second, the output performance of LL-TENG is also influenced by the parameters of topology-optimized leaf-like structure, such as leaf aspect ratio, leaf initial state curvature, and spacing between leaves, which should be studied respectively. Considering that the LL-TENG device is driven to achieve low cut-in wind speed under the action of gentle wind and to avoid over-damped vibration due to excessive mass of the counterweight piece, the mass of the counterweight piece should not be too heavy, the counterweight piece on top of LL-TENG leaf was designed to be 0.5, 1, 1.5, and 2 g for testing experiments, as shown in **Figure 3**a. The load on the counterweight piece at the top of the leaf increases continuously with

ADVANCED
SCIENCE NEWS
www.advancedsciencenews.com

ADVANCED
FUNCTIONAL
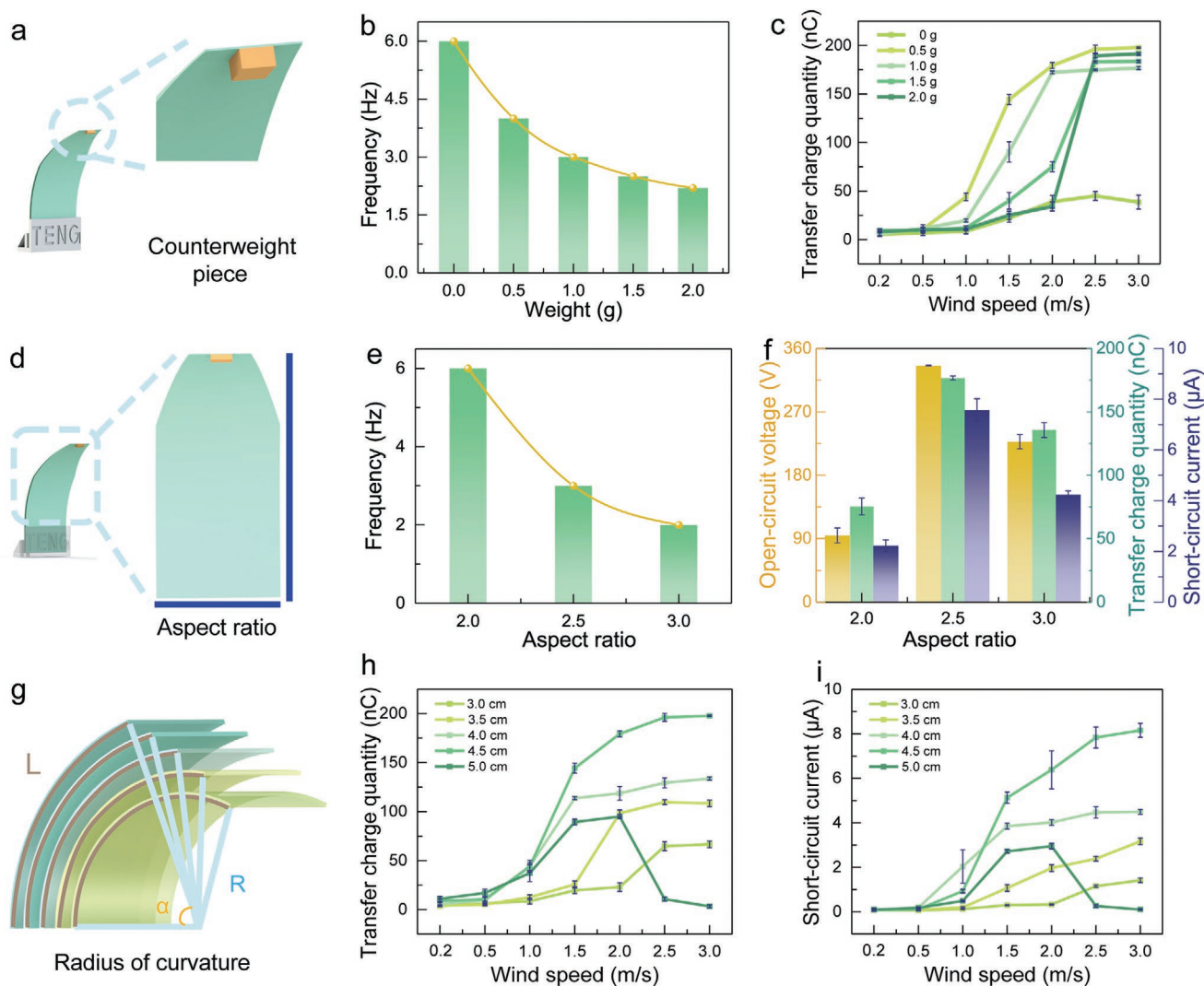**MATERIALS**
www.afm-journal.de

Figure 3. Structural parameters optimization of LL-TENG. a) Counterweight piece parameters of LL-TENG with topology-optimized leaf-like structure. b) Vibration frequencies of different counterweight pieces at a wind speed of 2.5 m s⁻¹. c) Transferred charge quantity (Qsc) of LL-TENG with different counterweight pieces and wind speeds. d) The aspect ratio of LL-TENG with topology-optimized leaf-like structure. e) Vibration frequencies of different aspect ratios at a wind speed of 2.5 m s⁻¹. f) Open-circuit voltage (Voc), transferred charge quantity (Qsc), and short-circuit current (Isc) of LL-TENG with different aspect ratios at a wind speed of 2.5 m s⁻¹. g) The radius of curvatures of LL-TENG. h) Transferred charge quantity (Qsc) and i) short-circuit current (Isc) of LL-TENG with different radius of curvatures and the wind speeds.

the spacing between the leaves, the aspect ratio of the leaves, and the initial state curvature of the leaves controlled. As can be seen in Figure 3b, the resonant frequency of LL-TENG device decreases with increased the weight of the counterweight piece, this is consistent with the results of the ω_0 analysis. At different wind speeds from 0.5 to 3.0 m s⁻¹, the best matching counterweight piece is 0.5 g. The reason is that when the counterweight piece is 0.5 g, it is not only effective in responding quickly to the impact of the wind but also has better output performance compared to others at different wind speeds, the electrical output performances of 198 nC, 338 V, and 7.9 μA were shown in Figure 3c and Figure S4a,b (Supporting Information). The phenomenon is that steady state damped forced vibration is an open dissipation system which continuously absorbs energy from the driving force source and at the same time dissipates capacity due to damping. When the dissipation capacity

increases until it is exactly the same as the absorbed energy, the system reaches a steady state. The lighter counterweight piece forms a smaller damping force and takes less time to move from the initial state to the steady state.

In addition, the output performance of LL-TENG can be improved by increased effective contact area. To clearly demonstrate, the electrical output of LL-TENG was studied with different structural parameters under the wind speed of 2.5 m s⁻¹ (by changing the aspect ratio of the topology-optimized leaf-like structure), as shown in Figure 3d. As shown in Figure 3e,f, the leaf width "D" is constant at 4 cm, the vibrational frequency of the LL-TENG device decreases with increased leaf lengths "L_1" (the length of 4, 8, and 12 cm), and the electrical output will first increase with the increased L and then decrease. The reason for this phenomenon is that a longer triboelectric layer can induce a greater contact area, however, the elasticity of the
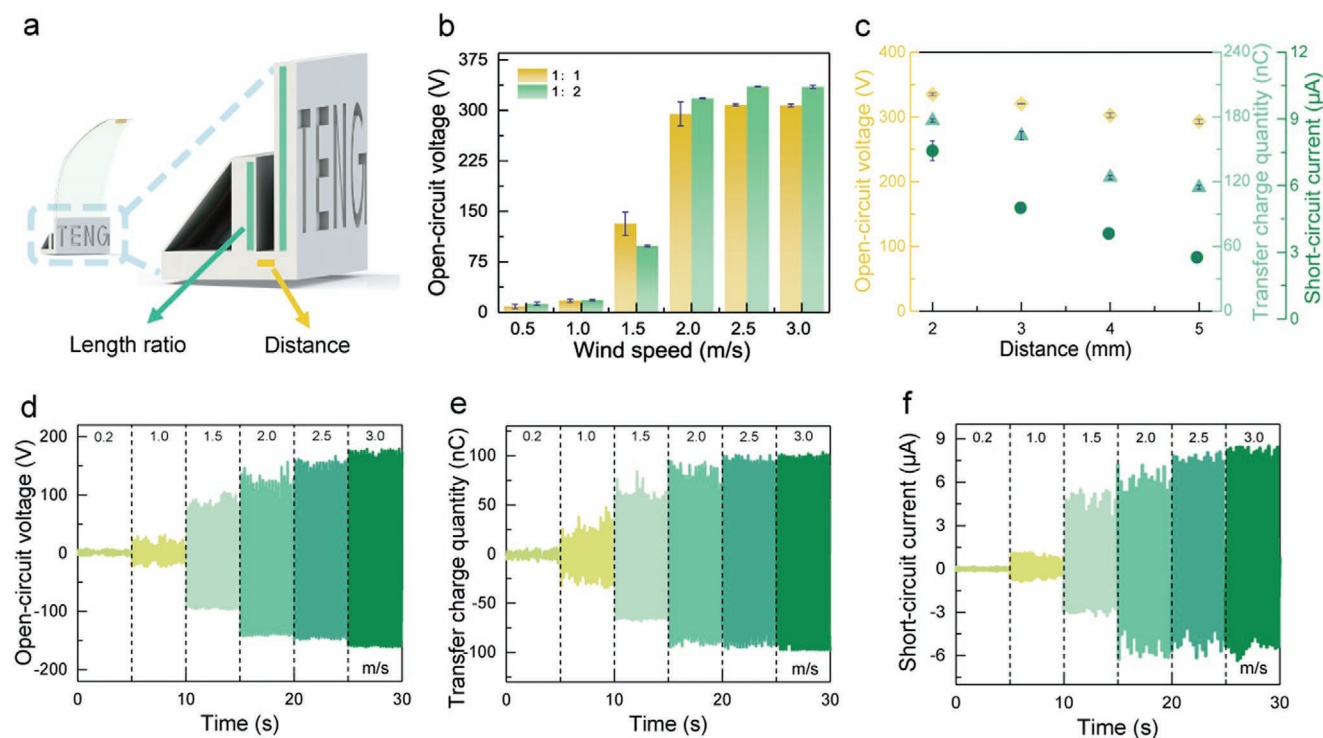
Figure 4. The electrical output performance of LL-TENG. a) Schematic diagram of LL-TENG's supporting base. b) Open-circuit voltage (Voc) of LL-TENG with different length ratio of support base and wind speeds. c) Open-circuit voltage (Voc), transferred charge quantity (Qsc), and short-circuit current (Isc) of LL-TENG with different distance at a wind speed of 2.5 m s^{-1}. d) Open-circuit voltage (Voc), e) transferred charge quantity (Qsc), and f) short-circuit current (Isc) of LL-TENG with different wind speeds at optimal parameters.

leaf decreases with the increased L, which hinders the effective separation of two triboelectric layers. Afterward, the initial state curvature of the leaf was changed with other conditions held constant for experimental comparison, and photographs of stainless-steel sheets with different curvatures are shown in Figure 3g. Here, the radius of curvature (R), arc length (L$_2$), and central angle (α) of the arc part satisfy the relationship (R = L$_2$/α). As depicted in Figure 3h,i and Figure S4c (Supporting Information), different R from 3.0 to 5.0 cm were employed to explore the output performance, which indicates that the optimal output performance can be obtained at R of 4.5 cm. This is due to the fact that with the increased curvature, the area of the leaf surface exposed to the wind becomes larger and the elasticity of the stainless-steel sheet is reduced, making it easier to separate between the two leaves. As the wind speed increases, the external drive is stronger than the recovery force of the stainless-steel sheet, prevent the leaf from oscillating periodically, resulting in a sudden drop in output. The output of LL-TENG increases with decreased R and abruptly at 5 cm. The LL-TENG leaf support base is shown in **Figure 4**a. By varying the support base for different length ratios and wind speed cases, it can be seen that the output performance is high and more stable at 1:2, as shown in Figure 4b. In addition, varying the base clearance distance reveals that the device performance decreases with increased the clearance, as shown in Figure 4c. Based on the above experimental results, the output performance of LL-TENG can be optimized with a counterweight piece of 0.5 g, a leaf aspect ratio of 1:2.5 (the wide of 4 cm and the long of 10 cm), a circular radius curva-

ture R of 4.5 cm, a support base with a length ratio of 1:2, and a clearance distance of 2 mm. At this set of structure parameters, the LL-TENG achieves maximum output performance of 338 V, 198 nC, and 7.9 µA at different wind speeds at a wind speed of 2.5 m s^{-1}, as shown in Figure 4d–f, respectively. The charge density transferred of 62.5 µC m^{-2} is reached on the effective contact area.

2.4. Electric Output Performance of LL-TENGs Array

A distributed power source (DPS) consists of the five LL-TENGs in parallel is developed by designed self-adaptive structure for all-round random gentle wind energy harvesting, including a full-wave rectifier bridge and a power management circuit (PMC).[11b] **Figure 5**ai shows a schematic diagram of DPS including the LL-TENGs array, rectifier bridge, and PMC. Figure 5aii shows the 3D structure drawing of DPS. In particular, the gas discharge tube (GDT) of PMC, is selected for use based on the high internal resistance and alternative-current output characteristics of the device, as well as the output. With the PMC, the problem of the device being unsuitable for directly powering electronic components can be effectively solved. The schematic illustration of PMC is shown in Figure S5 (Supporting Information), where the direct-current power after the full-wave rectifier bridge is applied into oscillation circuit through GDT and finally stored in the capacitor for load applications. As shown in Figure 5b, the number of LL-TENG units increases from 1 to 5. The V$_{OC}$ is remains constant

**ADVANCED
SCIENCE NEWS**

www.advancedsciencenews.com

**ADVANCED
FUNCTIONAL
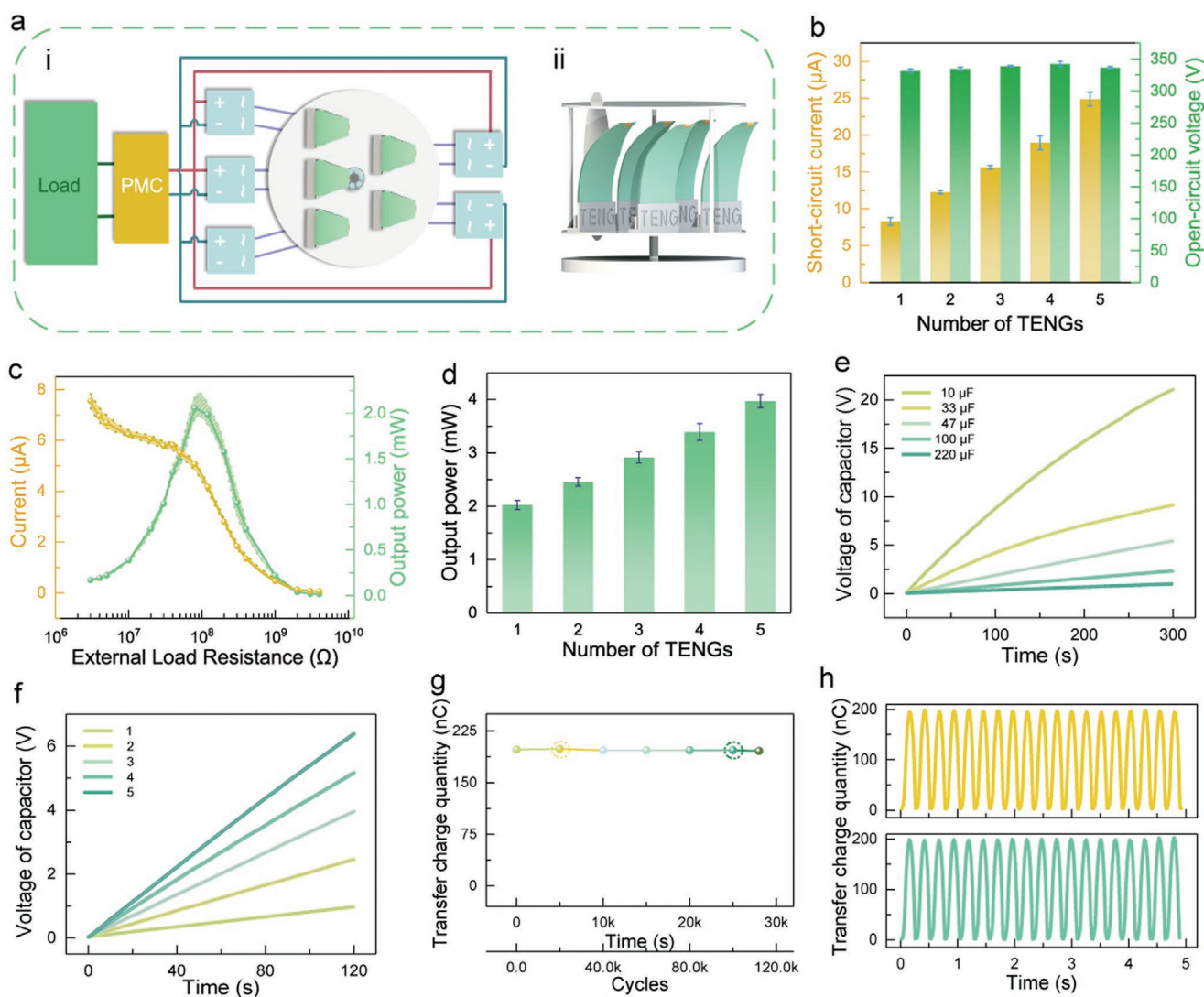MATERIALS**

www.afm-journal.de

Figure 5. Output performance of LL-TENGs network based on designed self-adaptive structure. a) The parallel connection of LL-TENG units through the rectified bridges and power management circuit (PMC). b) Open-circuit voltage (V_{oc}) and short-circuit current (I_{sc}) of LL-TENG with different numbers. c) The output power and instantaneous peak current-resistance relationship profiles for the LL-TENG. d) Output power of LL-TENGs from different number. e) Voltage profiles of the capacitor with different capacitance charged by the LL-TENG unit. f) Voltage profile of the 100 µF capacitor charged by the LL-TENGs with different number. g) Durability of LL-TENG based on the measurement of transferred charge quantity under 110000 cycles of operation. h) Enlarged view of durability test at 20000 cycles and 100000 cycles.

with the different number of LL-TENG units, while the I_{SC} increases from 7.9 to 24.3 µA.

To evaluate the matched impedance and the peak power of the LL-TENG device, its output performances are tested with a series of different load resistances at a wind speed of 2.5 m s^{-1}. As illustrated in Figure 5c, the output current has a horizontal trend when the resistance is small. Then the output current gradually decreases with increased the external load resistance, and the output power rise and then falls. A peak power of 2 mW is obtained under a load resistance of 80 MΩ. As shown in Figure 5d, a peak power of the DPS based on five LL-TENGs arrays reaches 3.98 mW, and the peak power increases linearly with increased the number of LL-TENG devices. In addition, the peak power at 0.2 m s^{-1} wind speed is shown in Figure S6 (Supporting information). It is thus conceivable that when a

sufficient number of DPSs are integrated, the transmission of the sensing information with long distances can be achieved in the desert (e.g., temperature and humidity sensors, wireless alarms, etc.). In addition, the DPS device has enough power to light 127 LEDs, as shown in Figure S7 (Supporting information). Moreover, the charging voltage of the capacitors with different number of LL-TENG units were investigated, as shown in Figure 5e,f. When operating at a wind speed of 2.5 m s^{-1}, the voltage of the capacitors from 10, 33, 47, and 100 µF are reached 21, 9.15, 5.44, 2.34, and 0.98 V in the charging time of 300 s, respectively. The voltage of 100 µF capacitor increases with increased the number of LL-TENG unit, and the value of voltage rise becomes faster in the same charging time. Furthermore, the output performance of LL-TENG was studied with the time of 7.8 h (more than 110 000 cycles) in continuous operation,

**ADVANCED
SCIENCE NEWS**

www.advancedsciencenews.com

**ADVANCED
FUNCTIONAL
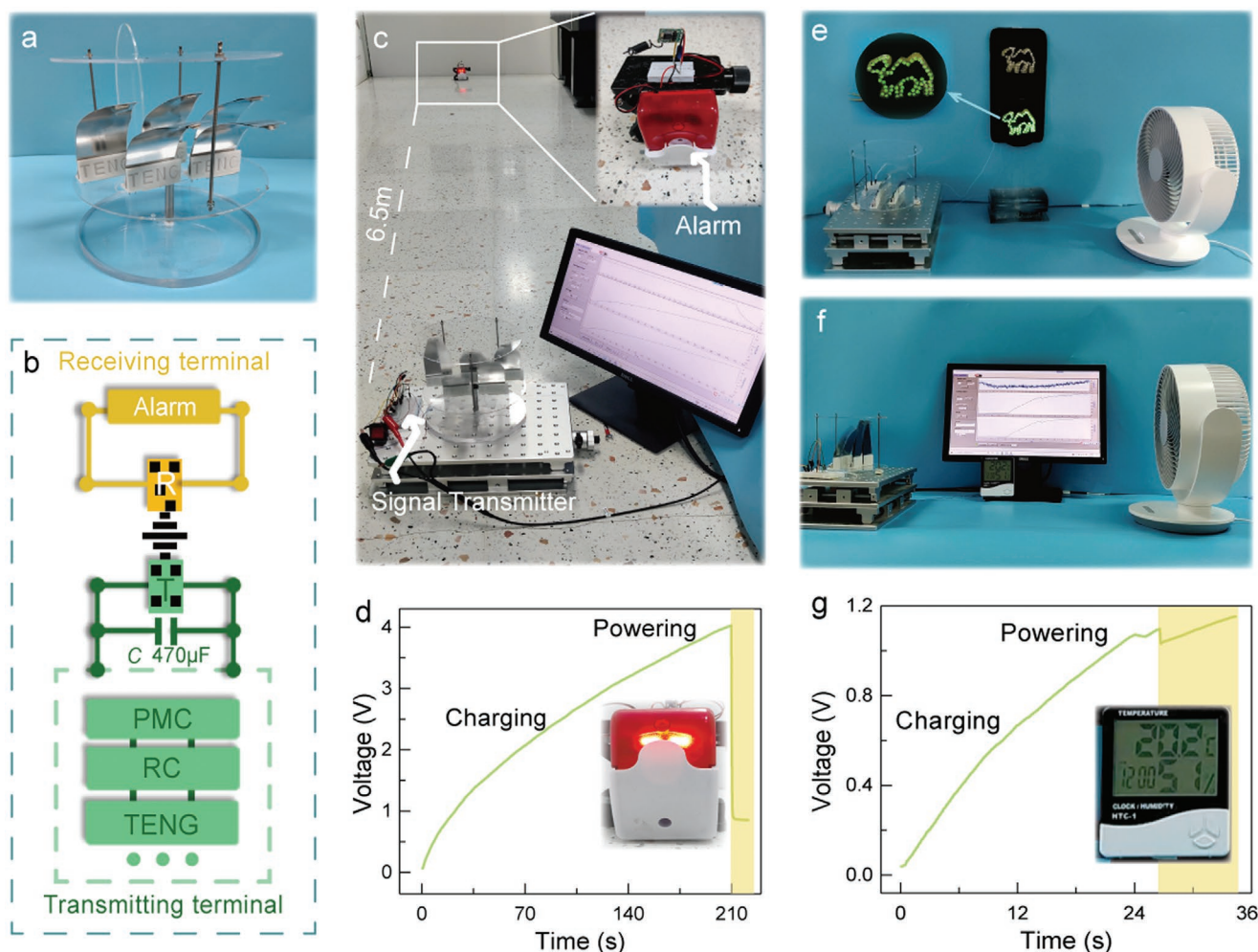MATERIALS**

www.afm-journal.de

Figure 6. Applications demonstration of distributed power source (DPS) based on the LL-TENGs network. a) Photograph of LL-TENGs network as a DPS. b) Circuit schematic of the self-powered system consisting of a DPS, power management circuit (PMC), rectifier bridge, capacitor, transmitter terminal, and receiver terminal. c) Photograph and demonstration of the self-powered emergency alarm system. d) Voltage profile of a self-powered emergency alarm system in the process of charging and discharging. e) Photograph and demonstration of the self-powered signal lights system. e) Photograph and demonstration of the self-powered signal lights system. f) Photograph and demonstration of the self-powered meteorological monitoring system. g) Voltage profile of the self-powered meteorological monitoring system in the process of charging and discharging.

the results are shown in Figure 5g,h, and Figure S8a,b (Supporting Information). Scanning electron microscope (SEM) images shown that the surface of the used FEP film has experienced light wear, which is not very different from the unused FEP film. The initial surface of the unused Al film had regular streaks due to the processing technology, and the streaks did not change much after use (Figure S8c,d Supporting Information). The results show that the transferred charge of LL-TENG retains still 97.5% after a continuous operating time of 7.8 h (Figure S9, Supporting Information), and the surface of FEP and Al film is lightly worn during the contact-separation process, which has very little effect on the output performances.

2.5. Practicability and Applications of LL-TENG

A self-powered emergency alarm system was developed, it has a simple structure consisting of the DPS, rectifier bridges, a PMC, a 470 µF capacitor, and signal transmitting unit, as shown in **Figure 6**a. The circuit schematic of the DPS is shown in Figure 6b. The working frequency of signal transmitting unit is 433.92 MHz. The photograph of the self-powered emergency alarm system and receiving terminal are exhibited in Figure 6c. In fact, the transmitting distance between the transmitter and the receiver may be tens or hundreds of meters, which is dependent on its transmission power and power supply. In the demonstration, a distance of 6.5 m is tested due to the space limitation of the laboratory. The voltage profile of the self-powered emergency alarm system in the process of charging and discharging, as shown in Figure 6d. When the charging time of the capacitor exceeds 210 s, the switch is closed and the transmitter is powered for sending a warning signal, then the remote signal receiver will be triggered and are given voice or the alarm signal light, as shown in Movie S4 (Supporting Information). In addition, a real-time self-powered signal light guidance system was developed for providing longest-distance

point-to-point assistance and clues to direction with geological survey personnel, explorers, vehicles, and camel caravan in the desert, as shown in Figure 6e and Movie S5 (Supporting Information). It can be a self-powered way to drive 127 LEDs and provide essential light or in the right direction to passers-by and vehicles at night in the wild. Furthermore, the meteorological monitoring technology can provide big data support for oil exploration, development, and production in the outdoors or desert, and plays an important role in basic support for desertification prevention and climate change research. A simple self-powered meteorological monitoring system was constructed by combining a commercial hygrothermograph, a DPS, rectifier bridges, a PMC, and a 470 µF capacitor, as shown in Figure 6f and Movie S6 (Supporting Information). The voltage profile of the self-powered meteorological monitoring system in the process of charging and discharging, as shown in Figure 6g. At a wind speed of 2.2 m s^{-1}, the operating voltage of the commercial hygrothermograph can be reached by the DPS within 26 s, which starts supplying power to the hygrothermograph and the display will always be illuminated. In conclusion, the applications of LL-TENG-based DPS by harvesting gentle wind energy for powering these low-power sensors is demonstrated, proves the effective and feasibility of LL-TENG as a self-powered distributed generation technology based on the contact electrification and structure optimization.

3. Conclusion

In summary, we reported a new leaf-like triboelectric nanogenerator (LL-TENG) based on damped forced vibration caused by the topology-optimized structure for high-effectively harvesting electrical energy from ultralow cut-in speed airflow/gentle wind energy. The LL-TENG is comprised of flexible leaves, leaf-like vein bearing plates, and counterweight pieces, that resemble plant leaves and derive effective output from low resonant frequency of damped forced vibration when driven by airflow or gentle wind. We study the effectiveness of topology-optimized leaf-like strategy, which solves the problem of reduced electrical output due to electrostatic adsorption between the leaf surfaces while the cut-in and rated wind speed reduced to 0.2 m s^{-1} and 2.5 m s^{-1}. The peak power of LL-TENG unit may reach 2 mW at a wind speed of 2.5 m s^{-1}. A distributed power source (DPS) consists of five-unit LL-TENGs network in parallel is developed by designed self-adaptive structure, which the peak power reaches 3.98 mW. Coupled with a power management circuit (PMC), the DPS may be utilized as a distributed direct-current power source for driving electronics. A set of applications include a self-powered emergency alarm system, a self-powered signal lights system, and a self-powered meteorological monitoring system were developed, respectively, and its practicability and durability are successful demonstrated for airflow/gentle wind energy harvesting in the desert. The effective and feasibility of LL-TENG was demonstrated as a self-powered distributed generation technology for the information transmission, data acquisition, and climate monitoring of large areas no man's land, and provides emergency alerts for the expedition, rescue, and human activities in the desert. This work proposes a novel topology-optimized strategy for harvesting gentle wind

energy of 0.2–2.5 m s^{-1}, with the deep-going research, we are looking at the possibility of wide application that the LL-TENG technology may be a potential complementary for wind turbines and distributed micro-nano energy in the future.

4. Experimental Section

Fabrication of LL-TENG: The base parts of LL-TENG were made by 3D printing (Tiertime up 300) with PLA material (Anycubic). The two leaves measure 10 cm (length) × 4 cm (width), with a PVC film (nearly 20 µm) on top and a 430 stainless-steel sheet (50 µm) on the bottom. The aluminum electrodes were pressed through the machine onto the PVC film and the FEP film was applied to the surface of the stainless-steel sheet. The stainless-steel sheet and the PVC film were each applied to the base support, after which the two electrodes were connected to the rectifier bridge. The distributed power source (DPS) consists of five LL-TENGs connected in parallel, supported by three parallel circular acrylic plates, connected to the shaft by means of bearings. A tailpiece was also added in the opposite direction of the device.

Characterization and Measurement: SEM was used to determine the microstructure of the samples (SU8020, Hitachi). The airflow was simulated by an electric fan. A commercial anemometer was used to measure wind speed. The Keithley 6514 system electrometer was applied to measure the electric output of LL-TENG. Airflow motion image on the LL-TENG surface measured by the schlieren photography (Luftvis). The base of LL-TENG was made by a 3D printer (Tiertime up 300). The dynamic stress analysis of LL-TENG was simulated at the mechanical condition and external airflow conditions by the software ANSYS.

Supporting Information

Supporting Information is available from the Wiley Online Library or from the author.

Acknowledgements

Conflict of Interest

The authors declare no conflict of interest.

Data Availability Statement

The data that support the findings of this study are available from the corresponding author upon reasonable request.

Keywords

[1] H. Peng, X. Fang, S. Ranaei, Z. Wen, A. L. Porter, *Nano Energy* **2017**, *35*, 358.

[2] Y. Li, E. Kalnay, S. Motesharrei, J. Rivas, F. Kucharski, D. Kirk-Davidoff, E. Bach, N. Zeng, *Science* **2018**, *361*, 1019.

[3] a) F.-R. Fan, Z.-Q. Tian, Z. L. Wang, *Nano Energy* **2012**, *1*, 328; b) J. Luo, Z. L. Wang, *Energy Storage Mater.* **2019**, *23*, 617; c) I.-W. Tcho, W.-G. Kim, S.-B. Jeon, S.-J. Park, B. J. Lee, H.-K. Bae, D. Kim, Y.-K. Choi, *Nano Energy* **2017**, *42*, 34; d) G. Zhu, Z. H. Lin, Q. Jing, P. Bai, C. Pan, Y. Yang, Y. Zhou, Z. L. Wang, *Nano Lett.* **2013**, *13*, 847; e) Z. L. Wang, T. Jiang, L. Xu, *Nano Energy* **2017**, *39*, 9; f) Z. L. Wang, *Faraday Discuss.* **2014**, *176*, 447.

[4] J. Han, Y. Feng, P. Chen, X. Liang, H. Pang, T. Jiang, Z. L. Wang, *Adv. Funct. Mater.* **2021**, *32*, 2108580.

[5] X. Liu, A. Yu, A. Qin, J. Zhai, *Adv. Mater. Technol.* **2019**, *4*, 1900608.

[6] S. Xu, G. Liu, J. Wang, H. Wen, S. Cao, H. Yao, L. Wan, Z. L. Wang, *Adv. Energy Mater.* **2021**, *12*, 2103408.

[7] a) C. G. Zhang, Y. B. Liu, B. F. Zhang, O. Yang, W. Yuan, L. X. He, X. L. Wei, J. Wang, Z. L. Wang, *ACS Energy Lett.* **2021**, *6*, 1490; b) W. Yang, P. J. Tavner, C. J. Crabtree, Y. Feng, Y. Qiu, *Wind Energy* **2014**, *17*, 673.

[8] a) J. Gubbi, R. Buyya, S. Marusic, M. Palaniswami, *Future Gener. Comput. Syst.* **2013**, *29*, 1645; b) Y. Wang, X. Liu, Y. Wang, H. Wang, H. Wang, S. L. Zhang, T. Zhao, M. Xu, Z. L. Wang, *ACS Nano* **2021**, *15*, 15700.

[9] C. Li, Y. Yin, B. Wang, T. Zhou, J. Wang, J. Luo, W. Tang, R. Cao, Z. Yuan, N. Li, X. Du, C. Wang, S. Zhao, Y. Liu, Z. L. Wang, *ACS Nano* **2017**, *11*, 10439.

[10] Y. Feng, L. Zhang, Y. Zheng, D. Wang, F. Zhou, W. Liu, *Nano Energy* **2019**, *55*, 260.

[11] a) Y. Luo, P. Chen, L. N. Y. Cao, Z. Xu, Y. Wu, G. He, T. Jiang, Z. L. Wang, *Adv. Funct. Mater.* **2022**, *32*, 2205710; b) Y. Liu, W. Yan, J. Han, B. Chen, Z. L. Wang, *Adv. Funct. Mater.* **2022**, *32*, 2202964.

[12] J. Zhang, Y. Sun, J. Yang, T. Jiang, W. Tang, B. Chen, Z. L. Wang, *ACS Appl. Mater. Interfaces* **2021**, *13*, 55136.

[13] a) X. Li, Y. Cao, X. Yu, Y. Xu, Y. Yang, S. Liu, T. Cheng, Z. L. Wang, *Appl. Energy* **2022**, *306*, 117977; b) I.-W. Tcho, W.-G. Kim, J.-K. Kim, D.-W. Kim, S.-Y. Yun, J.-H. Son, Y.-K. Choi, *Nano Energy* **2022**, *98*, 107197; c) X. Fu, S. Xu, Y. Gao, X. Zhang, G. Liu, H. Zhou, Y. Lv, C. Zhang, Z. L. Wang, *ACS Energy Lett.* **2021**, *6*, 2343; d) X. Zhang, J. Hu, Q. Yang, H. Yang, H. Yang, Q. Li, X. Li, C. Hu, Y. Xi, Z. L. Wang, *Adv. Funct. Mater.* **2021**, *31*, 2106527; e) L. Zhang, B. Meng, Y. Tian, X. Meng, X. Lin, Y. He, C. Xing, H. Dai, L. Wang, *Nano Energy* **2022**, *95*, 107029; f) J. Hu, X. Pu, H. Yang, Q. Zeng, Q. Tang, D. Zhang, C. Hu, Y. Xi, *Nano Res.* **2019**, *12*, 3018; g) P. Lu, H. Pang, J. Ren, Y. Feng, J. An, X. Liang, T. Jiang, Z. L. Wang, *Adv. Mater. Technol.* **2021**, *6*, 2100496; h) S. Yuan, Q. Zeng, D. Tan, Y. Luo, X. Zhang, H. Guo, X. Wang, Z. L. Wang, *Nano Energy* **2022**, *100*, 107465.

[14] Y. Wang, T. Chen, S. Sun, X. Liu, Z. Hu, Z. Lian, L. Liu, Q. Shi, H. Wang, J. Mi, T. Zhou, C. Lee, M. Xu, *Nano Res.* **2021**, *15*, 3246.

[15] a) Y. Chen, X. Mu, T. Wang, W. Ren, Y. Yang, Z. L. Wang, C. Sun, A. Y. Gu, *Sci. Rep.* **2016**, *6*, 2045; b) J. Wang, P. Liu, C. Meng, H. S. Kwok, Y. Zi, *ACS Appl. Mater. Interfaces* **2021**, *13*, 21450; c) S. Wang, X. Mu, X. Wang, A. Y. Gu, Z. L. Wang, Y. Yang, *ACS Nano* **2015**, *9*, 9554; d) S. Wang, X. Mu, Y. Yang, C. Sun, A. Y. Gu, Z. L. Wang, *Adv. Mater.* **2015**, *27*, 240.